The Astrophysical Journal, 1007:144 (9pp), 2026 August 20 https://doi.org/10.3847/1538-4357/ae8ba7

Spectroscopic Observations of 5303 Å Emission along a Preflare Solar Coronal Loop—Evidence for Plasma Upflows

R. Ramesh, V. Muthu Priyal, Jagdev Singh, K. Sasikumar Raja, P. Savarimuthu, E. Yuvashree, and S. Nagashree
Indian Institute of Astrophysics, Koramangala 2nd Block, Bangalore 560034, Karnataka, India
Received 2026 January 25; revised 2026 June 17; accepted 2026 July 8; published 2026 August 13

Abstract

The Visible Emission Line Coronagraph on board Aditya-L1 provides continuous spectroscopic observations of the solar corona in the Fe XIV 5303 Å emission line, which are a valuable tool to understand the plasma properties and dynamics in the near-Sun solar corona. One of the widely debated topics in the spectral line observations are the observed line widths, which are always in excess of the thermal width due to the ion temperature. In this context, we report estimates of the intensity, width, and Doppler velocity of the 5303 Å emission line along a preflare coronal loop in the heliocentric distance (r) range 1.10–1.24$R_\odot$. The Doppler velocity of the line shows a significant blueward shift (≈11 km s^{-1}) along one of the legs of the loop, indicating upflow of plasma. There is a simultaneous increase in the line width (≈0.2 Å) also. The changes in the above two parameters are strongly correlated. The correlation coefficient is ≈−0.9. The results indicate preflare activities are likely the cause for the excess line widths in the present case. The large change in the Doppler velocity, toward the blue side, confirms the related plasma upflows. The respective line parameters along either leg are nearly equal at the apex of the loop. The changes in the width and Doppler velocity in the other leg are comparatively minimal. The estimated upper limit for the Alfvén wave energy flux density at $r \approx 1.1R_\odot$ in the loop is ≈39%.

Unified Astronomy Thesaurus concepts: The Sun (1693); Solar corona (1483); Solar coronal loops (1485); Spectroscopy (1558); Solar coronal lines (2038)

1. Introduction

The Fe XIV 5303 Å forbidden spectral line, also called the "green" line, is the brightest and most prominent coronal emission line in the visible wavelength region of the electromagnetic spectrum. Its first observation was by C. A. Young (1872) during the total solar eclipse of 1869 August 7, and identification as Fe XIV line is due to W. Grotrian (1939). Spectroscopic observations provide details of the emission line parameters such as flux (intensity), line width, and Doppler velocity, which are important for investigating the physical and dynamic characteristics of the coronal plasma. Several authors have reported important results from such studies (T. Tsubaki 1975; H. Hara & K. Ichimoto 1999; I. S. Kim 2000; T. Sakurai et al. 2002; K. Hori et al. 2005; J. Singh et al. 2006a; I. Suzuki et al. 2006; S. Krishna Prasad et al. 2013; H. Tian et al. 2013; E. Landi et al. 2016; A. Ding & S. R. Habbal 2017; S. Koutchmy et al. 2019; G. D. Muro et al. 2023; R. Ramesh et al. 2024; Y. Zhu et al. 2024; V. Muthu Priyal et al. 2025a, 2025b). The full width at half-maximum (FWHM), simply mentioned as width, of a coronal emission line varies because of variations in the temperature and/or nonthermal velocity of the coronal plasma. The excess in the FWHM of the line, beyond the value expected based on the thermal properties of the emitting ion (thermal broadening) and the instrumental properties (instrumental broadening), has been interpreted as nonthermal broadening. It may be due to microscale turbulence or integrated emission from multiple overlapping coronal structures along the line of sight (LoS).

The results of spectroscopic observations in the 5303 Å emission line carried out during eclipses and ground-based coronagraphs by different observers led to different scientific interpretations. H. Hara & K. Ichimoto (1999) found that the FWHM of coronal emission lines for the edge-on loop appears to become smaller near the loop top compared to the face-on loops. They also reported different values of nonthermal velocities for the 5303, 5694, and 6374 Å emission lines. L. Contesse et al. (2004) found no variations in the FWHM of the 5303 Å emission line beyond 120″ above the solar limb. Further, the authors obtained different line widths for different coronal regions. J. Singh et al. (2006a, 2006b) carried out systematic spectroscopic observations in the 5303, 6374, 7892, and 10747 Å emission lines for long periods on a number of days in different coronal regions with the 25 cm Norikura coronagraph. They reported that the width of the 5303 Å emission line decreased up to height of ≈200″ above the limb and thereafter remained same up to ≈500″ height. Also, they found that the FWHM of the emission line and its gradient with height are different in different coronal regions. Observations in the 5303 Å emission line by J. Singh et al. (2011) during the total solar eclipse of 2009 July 22 indicate a gradual increase in the FWHM in the distance range 1.15–1.5$R_\odot$. Observations with the Large Angle and Spectroscopic Coronagraph C1 (LASCO C1) on board the Solar and Heliospheric Observatory indicate that in the year 1996, the FWHM of the 5303 Å line increased with height up to ≈1.3$R_\odot$ and then decreased until ≈1.5$R_\odot$, whereas in 1998, the FWHM remained roughly constant (M. Mierla et al. 2008). Observations by Y. Zhu et al. (2024) during the 2017 August 21 total solar eclipse show that 5303 Å dominates in the closed fields of an active region and the base of a streamer. The nonthermal velocity corresponding to the line width is in the range 20–30 km s^{-1} (≈0.90–1.12 Å), independent of the height.

G. D. Muro et al. (2023) reported Doppler velocity (bulk plasma motion) ranging from −12 to +2.5 km s^{-1}, using 5303 Å emission line observations at the base of a streamer, within ≈0.4$R_\odot$ above the solar limb. B. Q. Zhu et al. (2025) reported that emission in the 5303 Å line shows a blueshift of ≈−2 km s^{-1} in the "quiet" inner corona at a higher latitude (60°N) and ≈−6 km s^{-1} at the base of a helmet streamer in the lower latitude (35°N).

There are vast amounts of literature on observations in the 5303 Å solar coronal emission line, some of which are mentioned in the previous two paragraphs, but reports and analysis of combined observations of the different line parameters (i.e., intensity, FWHM, Doppler velocity) as a function of height above the solar limb are limited (T. Tsubaki 1983; H. Hara & K. Ichimoto 1999; T. Sakurai et al. 2002). Observations of loop structures are expected to be useful in this regard since they are the basic building blocks of the solar corona. The coronal loops in the solar atmosphere are the manifestations of magnetic field confining the plasma and allowing movement along the field lines. Investigation of simple loop structures in the "quiet" corona is important to understand more complex and dynamic structures in the "active" corona (see, e.g., G. Del Zanna & H. E. Mason 2003). We report observations of one such well-defined coronal loop structure in this work using 5303 Å data obtained with the Visible Emission Line Coronagraph (VELC) on board Aditya-L1, taking advantage of its continuous spectroscopic observations of the solar corona from the Sun–Earth Lagrangian L1 location (J. Singh et al. 2025).

2. Instrument and Observations

2.1. Aditya-L1/VELC

The VELC payload on board Aditya-L1 is an internally occulted solar coronagraph with capability to carry out multislit spectroscopic observations using four straight slits; thereby four different regions of the solar corona are observed simultaneously (J. Singh et al. 2025). There are two observational modes in VELC: "sit-stare" and "raster scan." The sit-stare mode observes the solar corona at a fixed position for a chosen time and interval, while the raster mode scans the solar corona from −1.5 to +1.5$R_\odot$ (from east to west). The scan ranges from −1.5 to −0.75$R_\odot$ for slit 1, from −0.75 to 0$R_\odot$ for slit 2, from 0–0.75$R_\odot$ for slit 3, and from 0.75–1.5$R_\odot$ for slit 4. Note the location of the VELC occulter edge in the corona gradually varies in a periodic manner due to seasonal changes in the apparent size of the Sun and fixed size of the occulter in VELC. The edge will correspond to $r \approx 1.04R_\odot$ in early January of any given year. The location gradually increases to a maximum of $r \approx 1.07R_\odot$ in July the same year and then slowly returns to $r \approx 1.04R_\odot$ in January of the following year.

The instrument details related to the present observations are shown in Table 1. The slit width of the spectrograph, equivalent to 9$''$.6, limits the spatial resolution in the east–west direction. Therefore, we average data along the slits to have comparable resolution in the north–south direction also. Details of the methodology used to extract the emission line parameters are described in V. Muthu Priyal et al. (2024, 2025a) and J. Singh et al. (2025). In brief, the data reduction procedure involves (i) preprocessing of raw spectra, dark subtraction, flat-field correction, and scattered light correction; (ii) Gaussian fitting to the observed emission lines for extracting parameters such as peak intensity, Doppler velocity, and emission line width; and (iii) correction for instrumental broadening. Before the launch of VELC on board Aditya-L1, in the laboratory, we have obtained the spectrum using a solar beam. Using the photospheric absorption lines at 5302.307 and 5300.751 Å, we found that the dispersion is 28.4 mÅ per pixel. The FWHM of these absorption lines, 0.272 ± 0.03 Å, indicates the width of the instrumental profile (R. P. Budihal et al. 2023). The slit width of 50 μm, which corresponds to 219 mÅ, dominates the instrumental profile. The natural width of the absorption line also contributes to the measured instrumental profile. We have taken the Sun disk light spectra after the launch also. The emission spectra of the solar corona, too, show these absorption lines due to scattering of the Sun disk light by the optical components. Using these spectra, we again determined the values of dispersion and line width of the absorption lines. The values measured in orbit agree with those measured in the laboratory. Hence, we use 0.272 Å as the instrumental width to correct the measured line width of the emission line. We have considered the wavelength of the absorption line 5302.307 Å and dispersion of 28.4 mÅ per pixel to determine the average central wavelength of the emission line. The value is 5302.8 ± 0.02 Å, which agrees with similar estimates from a large number of high-spectral-resolution observations using the Norikura and Sacramento Peak Observatory coronagraphs (T. Tsubaki 1975; J. Singh et al. 2004, 2006a). Therefore, we use 5302.8 Å (corresponding to 5304.3 Å in a vacuum, G. Del Zanna & E. E. DeLuca 2018) as the mean wavelength of the emission line to compute the Doppler velocity. It may be noted that the spectral dispersion and mean wavelength mentioned above are average values, computed from a large number of observations. Their standard deviations are small, ≈0.1 mÅ and ≈0.02 Å, respectively. By stacking the emission line parameters measured from the observed spectra at different spatial positions, two-dimensional coronal maps are generated.

Table 1
Instrument Details Related to the Observations

Parameter	Specifications
Occulter radius ($R_\odot$)	1.06
Field of view (FoV) ($R_\odot$)	1.05–1.50
Spatial scale (arcsec per pixel)	1.25
Number of slits	4
Separation between slits (mm)	3.75 (equivalent to 12$'$)
Slit width (μm)	50 (equivalent to 9$''$.6) east–west direction of the Sun
Slit length (mm)	15 (equivalent to 48$'$) north–south direction of the Sun
FoV (each slit position) ($R_\odot$)	±1.5 × 0.01 (spatial direction × dispersion direction)
Spectral dispersion (mÅ per pixel)	28.4
Raster scan range ($R_\odot$)	0.75 (simultaneous for each slit)
Scan step (μm)	40 (7$''$.7 in the image plane)
Number of scan steps	95
Scan duration (minute)	35

2.2. Data

For the present study, raster scan spectroscopic observations in the Fe XIV (5303 Å) emission line carried out on 2025

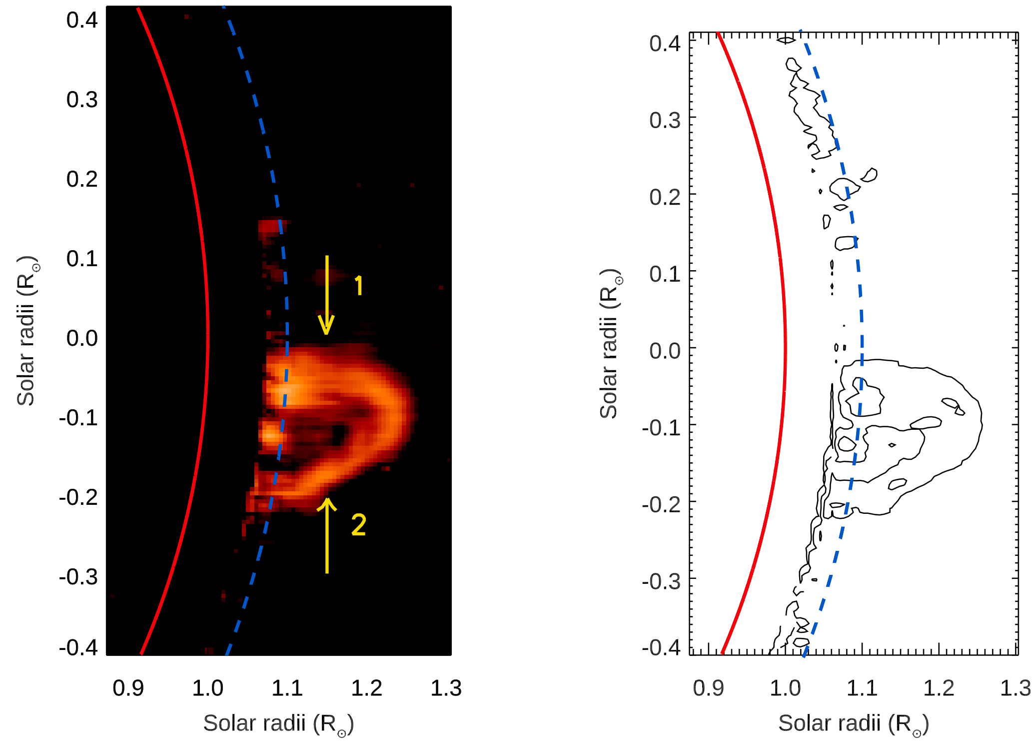

Figure 1. Left panel: coronal image on the west limb of the Sun in the 5303 Å emission line on 2025 October 5 obtained during the period 22:50–23:25 UT, using raster scan observations with VELC. The red arc represents the solar limb. The black area with circular edge in the image is the VELC occulter ($r = 1.06R_{\odot}$). The blue dashed line is at $r = 1.10R_{\odot}$ (see Section 3.1 for details). Solar north is straight up, and east is to the left. The bright structure close to the occulter edge in the southwest quadrant is the coronal loop discussed in the main text. Yellow arrows 1 and 2 indicate the upper and lower legs of the loop, respectively. Right panel: contour version of the coronal image in the left panel, showing the outline of the loop.

October 5 are used. The exposure time for each frame is 4 s, with 1x detector gain. At each step, five frames were acquired and binned to save as a single frame on board to improve the signal-to-noise ratio (SNR). The onboard binning helps to reduce the data volume for transmission to the ground and thereby enables more observations. The time interval between successive raster steps is 20 s. The raster scan image generated using the peak emission line intensity corresponding to slit 4 (at the west limb) during the period 22:50–23:25 UT on 2025 October 5 is shown in Figure 1. A coronal loop structure can be prominently seen. The loop is asymmetric with an inclined lower leg and a comparatively straight upper leg (see, e.g., T. Sakurai et al. 2002). The associated sunspot region is NOAA 14230 located at the heliographic coordinates S11W88. The Geostationary Operational Environmental Satellite (GOES) observed a weak, C1.9 class soft X-ray flare from the above region during the period 23:38–00:34 UT, with the peak at 23:57 UT. No flare activity was reported during the VELC observing period mentioned above.[1] In Figure 1, the upper leg (1) of the VELC loop appears more broader than the lower leg (2). To verify this, we inspected the 211 Å image of the corona obtained on 2025 October 5 at ≈23:28 UT with the Atmospheric Imaging Assembly (AIA; J. R. Lemen et al. 2012) on board the Solar Dynamics Observatory (SDO; Figure 2). It shows multiple loops, spaced apart in the region of the VELC slit, near the upper leg (1) of the VELC loop. The 211 Å loops near the lower leg (2) of the VELC loop are comparatively more closely spaced. Due to low spatial resolution of the VELC, the multiple spaced-apart loops in the 211 Å image appear like a broad structure in the VELC observations, i.e., upper leg (1).

3. Results and Discussions

3.1. Emission Line Parameters

Figure 3 shows the line profiles and associated fitted Gaussian profiles at different distances along the lower and upper legs of the loop in Figure 1. The line profiles and parameters correspond to the midsection (≈25″ wide in the spatial direction) in both loop legs. The average value minimizes any possible ambiguities due to the difference in the sizes of the two legs of the loop. We also calculated the peak flux, width, and Doppler velocity of the 5303 Å emission for the coronal loop structure in Figure 1 in the distance range $r = 1.10$–$1.24R_{\odot}$. In order to avoid possible confusion due to intense emission close to the occulter edge (see, e.g., L. Contesse et al. 2004), we considered the line parameters from $1.10R_{\odot}$ (indicated by the blue color arc in Figure 1), away from the VELC occulter edge at $1.06R_{\odot}$. The results of our calculations are shown in Figure 4. The upper, middle, and lower panels show the line intensity, line width, and Doppler velocity, respectively. Figure 5 shows the corresponding noise-filtered images of the loop structure, generated by considering only the data points whose amplitudes are greater than 5σ, where σ is the variance in the data. The line intensity in the upper leg of the loop shows a decrease from 16 ± 2 erg s^{-1} cm^{-2} Å^{-1} sr^{-1} at $1.10R_{\odot}$ to 9.5 ± 1.5 at $1.15R_{\odot}$. Then, it increases to 11 ± 1.5 at $1.21R_{\odot}$ and subsequently decreases to 8 ± 1.5 near the apex of the loop at $1.24R_{\odot}$. The line intensity in the lower leg exhibits the

[1] https://solarmonitor.org/?date=20251005

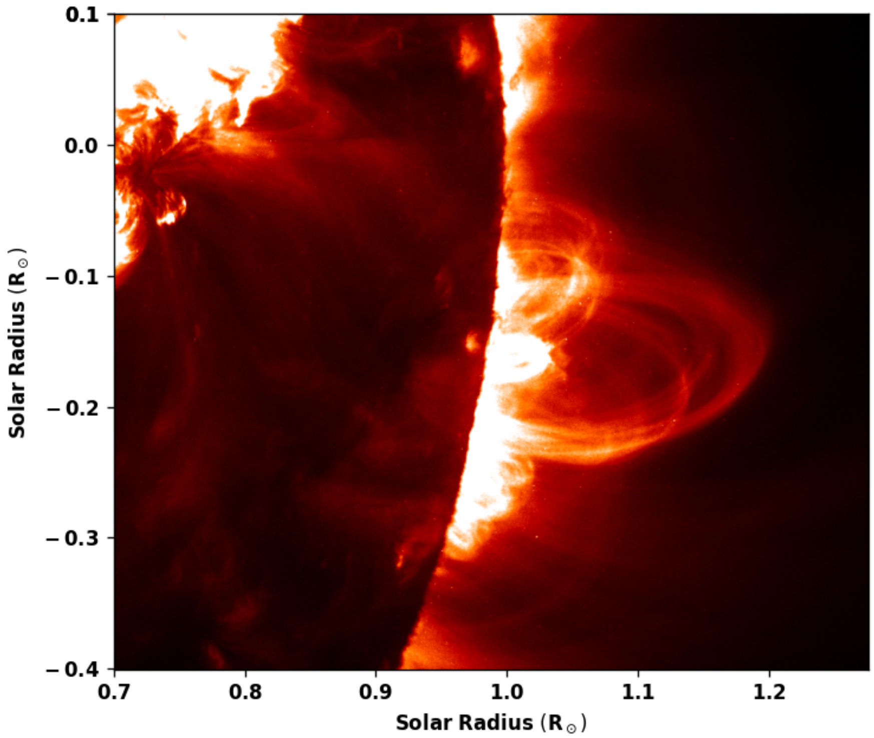

Figure 2. A close-up view of NOAA 14230 and the coronal loops in the SDO/AIA 211 Å observations.

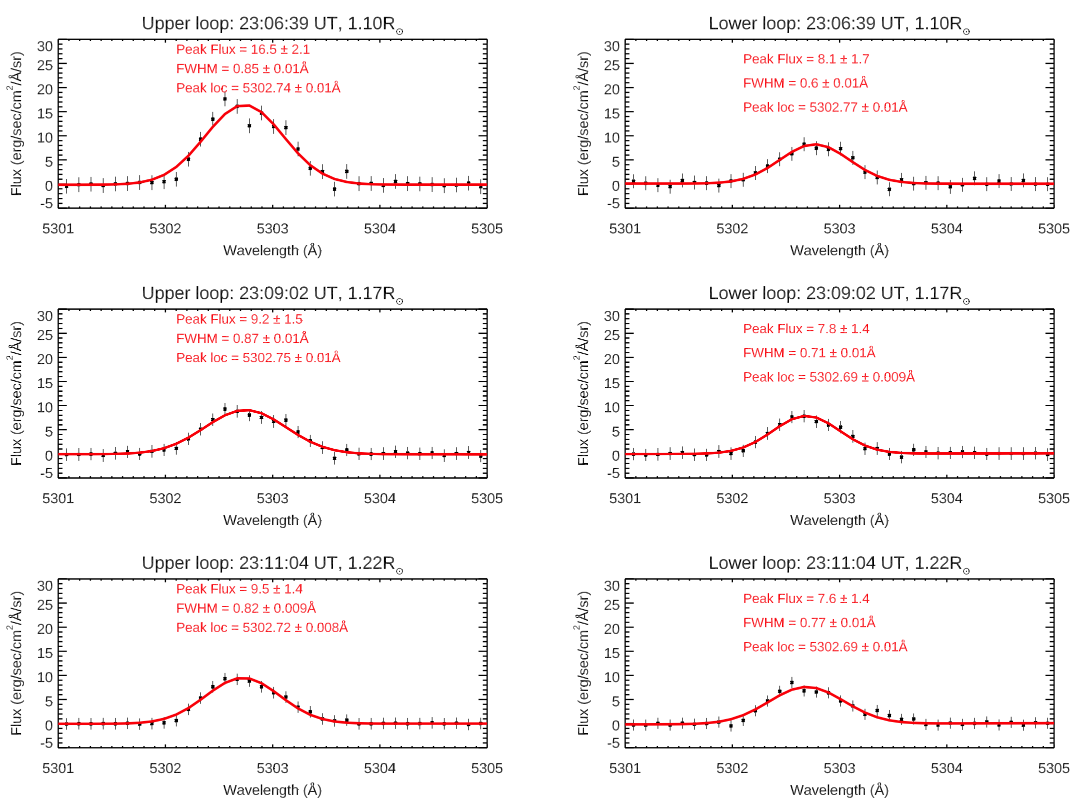

Figure 3. Spectral profiles corresponding to the upper and lower legs in the coronal loop in Figure 1, at different distances along the two legs. The peak emission flux and line width at each epoch (corresponding to the slit position in the raster scan) and distance are mentioned.

opposite trend. It increases from 8 ± 2 erg s^{-1} cm^{-2} $Å^{-1}$ sr^{-1} at 1.10$R_\odot$ to 9.5 ± 1.5 at 1.15$R_\odot$, decreases to 7 ± 1.5 at 1.21$R_\odot$, and increases to 8 ± 1.5 at 1.24$R_\odot$. The magnitude of change is greater in the upper leg in the distance range 1.10–1.15$R_\odot$, likely due to the bright emission near the occulter edge in the upper leg (Figure 1) and multiple spaced-apart loops as mentioned earlier (Section 2). Similarly, the noticeable changes in the line parameters of the lower leg close

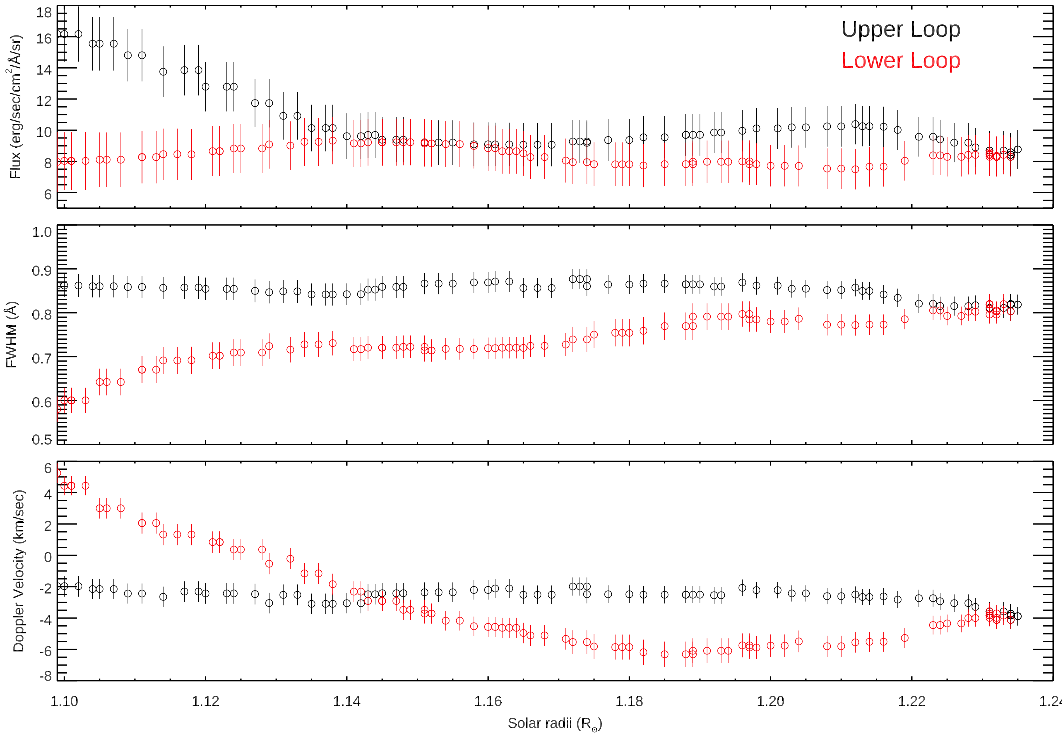

Figure 4. The upper panel shows the variation in the 5303 Å emission line flux along the upper and lower legs of the loop (Figure 1) in the distance range 1.10–1.24$R_\odot$. The values for the upper and lower loops are shown in black and red, respectively. The corresponding width and Doppler velocity are shown in the middle and lower panels, respectively. The vertical extent of the line on each data point indicates the magnitude of the uncertainties in the estimates.

to ≈1.14$R_\odot$ are probably due to the change in its inclination at the above distance (Figure 1). In the case of line width, the values in the upper leg are more or less uniform at 0.86 ± 0.02 Å in the distance range 1.10–1.21$R_\odot$. Afterwards, it decreases to 0.81 ± 0.02 Å at 1.24$R_\odot$. The line widths in the lower leg show a near-gradual increase from 0.60 ± 0.02 Å at 1.10$R_\odot$ to 0.77 ± 0.02 Å at 1.19$R_\odot$. It increases to 0.81 ± 0.02 Å near 1.24$R_\odot$. The Doppler velocity in the upper leg shows a trend similar to the line width. It is nearly the same at −2 ± 0.6 km s^{-1} in the distance range 1.10–1.21$R_\odot$ and decreases to −4 ± 0.6 km s^{-1} at 1.24$R_\odot$. Compared to this, there is a larger change in the lower leg. The Doppler velocity decreases from 5 ± 0.6 to −6 ± 0.6 km s^{-1} in the distance range 1.10–1.19$R_\odot$. Subsequently, it increases to −4 ± 0.6 km s^{-1} at 1.24$R_\odot$. The line intensities in the two legs are in reasonable agreement with the recently reported estimates from total solar eclipse observations in 5303 Å (B. Boe et al. 2026). Similarly, the line widths are in the range of values obtained from Norikura coronagraph and eclipse observations (J. Singh et al. 2006b; S. Koutchmy et al. 2019).

Note that the changes in the emission line parameters mentioned above should be treated with caution since the SDO/AIA 211 Å observations in Figure 2 indicate the presence of multiple loop structures with different loop lengths near the loop structure seen in the VELC observations (Figure 1) and the low spatial resolution of the VELC as mentioned in Section 2.2. The uncertainties in the emission line parameters include photometric errors in the raw data, errors in the dark and flat, errors in the Gaussian fit for the emission line, and errors in the wavelength and velocity calibration. The photometric errors are dominant. They affect primarily the line intensities. The uncertainties in the case of line widths and Doppler velocities are chiefly due to the Gaussian fitting errors, hence, the comparatively larger error bars for the line intensities in Figure 4. The minimal changes in the line width and Doppler velocity in the upper leg as compared to the lower leg (Figure 4) indicate differences between the activities in the two legs, likely due to asymmetry in the energy releases. Figure 2 shows crossover of multiple loops near both legs of the loop structure in Figure 1, but the larger changes in the line width and Doppler velocity are seen in the lower leg only as mentioned above. This strengthens the above suggestion that differences in the energy releases between the two legs are the likely cause for the differences between the changes in the respective line parameters in the two legs of the loop. The heated coronal plasma moves primarily along and/or parallel to the magnetic field lines, since the gas pressure is much less than the magnetic pressure in the solar corona. There is no cross-field diffusion. The variation in the parameters of a coronal loop may depend on the activities at its footpoints of the loop (e.g., magnetic reconnection, L. P. Chitta et al. 2018). The lower and upper legs of the loop have different footpoints. The activities in the two footpoints are likely to be different and vary with time. So, the emission line parameters in the upper leg of the coronal loop in the present case are uninfluenced by the changes in the corresponding parameters in the lower leg.

3.2. Effective Temperature and Nonthermal Velocity of the Emission Line

From Section 3.1, we find that the respective line parameters in the two legs, close to the loop apex, are nearly equal, likely due to mixing of plasma (see, e.g., J. Singh et al. 2019). The intensity values in either leg of loop are lower compared to similar values reported in our earlier study (R. Ramesh et al. 2025). The effective temperature ($T_{\rm eff}$), comprising of thermal

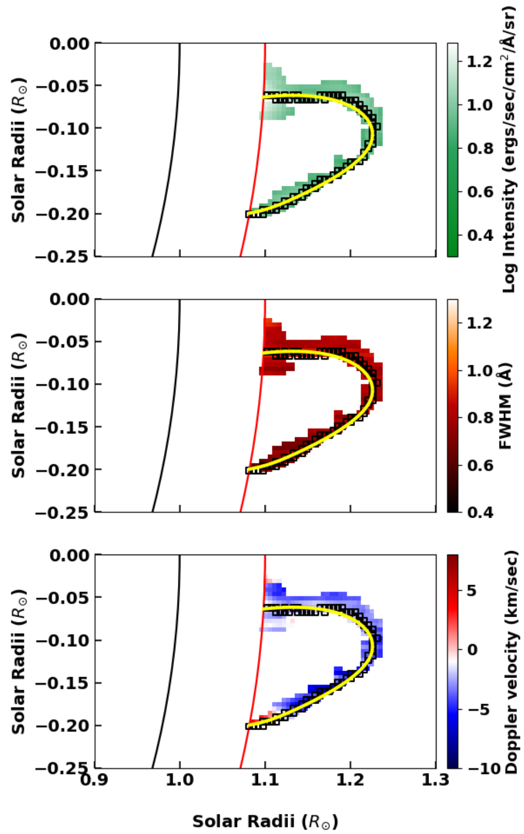

Figure 5. Noise-filtered, close-up view of the intensity, FWHM, and Doppler images of the coronal loop structure in Figure 1. The black arc represents the solar limb. The red arc is at $r = 1.10R_\odot$. Coronal emission between $r = 1.06R_\odot$ (occulter edge) and $r = 1.10R_\odot$ are masked to show the loop structure clearly. The data points in Figure 2 are the average values inside the black square boxes shown along either leg of the loop in all the above three images. The yellow lines are the least-squares fits for the aforesaid boxes in each image. The redshift in the Doppler velocity in the lower leg of the loop, until $\approx 1.13R_\odot$ (Figure 4), can be noticed here also.

and nonthermal contributions, is calculated from the line width using the relation, $T_{\rm eff} = \frac{mc^2}{2k_{\rm B}}\left(\frac{w}{2\sqrt{\ln 2}\,\lambda}\right)^2$, where $m = 9.33 \times 10^{-26}$ kg is the Fe XIV ion mass, $k_{\rm B}$ is the Boltzmann constant, w is the FWHM of the line, and $\lambda = 5303$ Å. In the present case, $T_{\rm eff}$ in the upper leg is nearly steady at $\approx 2.9 \times 10^6$ K. In the lower leg, $T_{\rm eff}$ shows a gradual increase from $\approx 1.4 \times 10^6$ K to $\approx 2.9 \times 10^6$ K, toward the apex of the loop. Eclipse observations in the 5303 and 7892 Å emission lines indicate that the minimum electron temperature (T_e) in the regions of the closed magnetic field lines can be $\approx 1.2 \times 10^6$ K (B. Boe et al. 2020). Since T_e and the ion temperature (T_i, the thermal component in $T_{\rm eff}$) are generally assumed to be equal, the excess in $T_{\rm eff}$ beyond $\approx 1.2 \times 10^6$ K can be considered as the nonthermal component in the present case. Assuming $\approx 1.2 \times 10^6$ K for T_i in the present case, we calculated the nonthermal velocities corresponding to the line widths shown in the middle panel of Figure 4 using the relation, $\left[\left(\frac{w}{\lambda}\right)^2 \frac{c^2}{4\ln(2)} - \left(\frac{2k_{\rm B}T_i}{m}\right)\right]^{1/2}$. The nonthermal velocities increase from ≈ 19 km s^{-1} (at $\approx 1.10R_\odot$) to ≈ 27 km s^{-1} (at $\approx 1.24R_\odot$) in the lower leg of the loop. The corresponding increase in the excess $T_{\rm eff}$, beyond 1.2×10^6 K, is ≈ 0.2–1.7×10^6 K. In the case of the upper leg, the nonthermal velocities are nearly uniform, ≈ 27–29 km s^{-1}, between $\approx 1.10R_\odot$ and $\approx 1.24R_\odot$. The above values are in reasonable agreement with the nonthermal velocities of ≈ 20–30 km s^{-1} for plasma motions near the footpoints of active region coronal loops observed with the EUV Imaging Spectrometer (EIS) on board Hinode (see, e.g., H. Hara et al. 2008).

3.3. Preflare Activity

There was a C1.9 class GOES soft X-ray flare ≈ 13 minutes after our observations (Section 2.2). So, the preflare activities in the region are probably the common driver behind the observed line widths, Doppler velocities, and their variations. We verified this using VELC sit-stare observations in 5303 Å carried out on the same day (i.e., 2024 October 5) at the west limb of the occulter, until 22:40 UT, just prior to the VELC raster scan observations in Figure 1, and SDO/AIA 211 Å observations. The VELC sit-stare emission, from nearly the same location as the coronal loop structure in Figure 1, shows a gradual increase in the intensity from $\approx$21:50 UT until the end of the observations at 22:40 UT (Figure 6). The last reported GOES soft X-ray flare from the solar limb close to the coronal loop, prior to $\approx$21:50 UT, is at $\approx$18:50 UT. The ≈ 3 hr time difference rules out the possibility of any flare association with the abovementioned intensity increase in the VELC sit-stare emission. So, it is likely due to preflare activities like heating, structural changes, and magnetic field changes prior to the onset of the C1.9 flare from 23:38 UT in this case (see, e.g., A. Bruzek & H. L. Demastus 1970; S. F. Martin 1980). The SDO/AIA 211 Å observations shows a gradual and almost equal increase in intensity near the footpoints of both the upper and lower legs during $\approx$21:50–22:50 UT (Figure 6). The near-simultaneous intensity increase, ≈ 108 minutes prior to the flare, in two different observing wavelengths with two different instruments, indicates a common origin for them, i.e., the preflare activity in the present case. The preflare activity reported in A. Bruzek & H. L. Demastus (1970) is ≈ 75 minutes before the flare onset. We find that while the 211 Å intensity in the lower leg shows a continued increase during the VELC raster scan time (22:50–23:25 UT) also, it remains nearly the same beyond $\approx$22:50 UT in the upper leg. This difference between the 211 Å activities near the base of the two legs of the loop during the VELC raster scan time is consistent with our argument in Section 3.1 that larger variations in the FWHM and Doppler velocity in the lower leg of the loop as compared to its upper leg are due to asymmetry in the energy releases between the two legs.

3.4. Plasma Flows

G. A. Doschek et al. (2008) showed that there can be significant Doppler shifts and line widths even in regions of low intensity, which is true in the present case also. There are considerable changes in the line width and Doppler velocity in the lower leg of the loop, despite its lower intensity. The changes are at the same time, with $\approx 90\%$ inverse correlation. The correlation coefficient is ≈ -0.9 (Figure 7). The simultaneous changes indicate that the values of both the above line parameters as well as the trend exhibited by them are due to the same activity. The correlation is inverse because the Doppler velocities are increasingly negative (i.e., more blueshifted) along the loop, as compared to the line width. Blueshift corresponds to upflows caused by heating (see, e.g., H. Hara et al. 2008). Reports indicate that there can be reversal

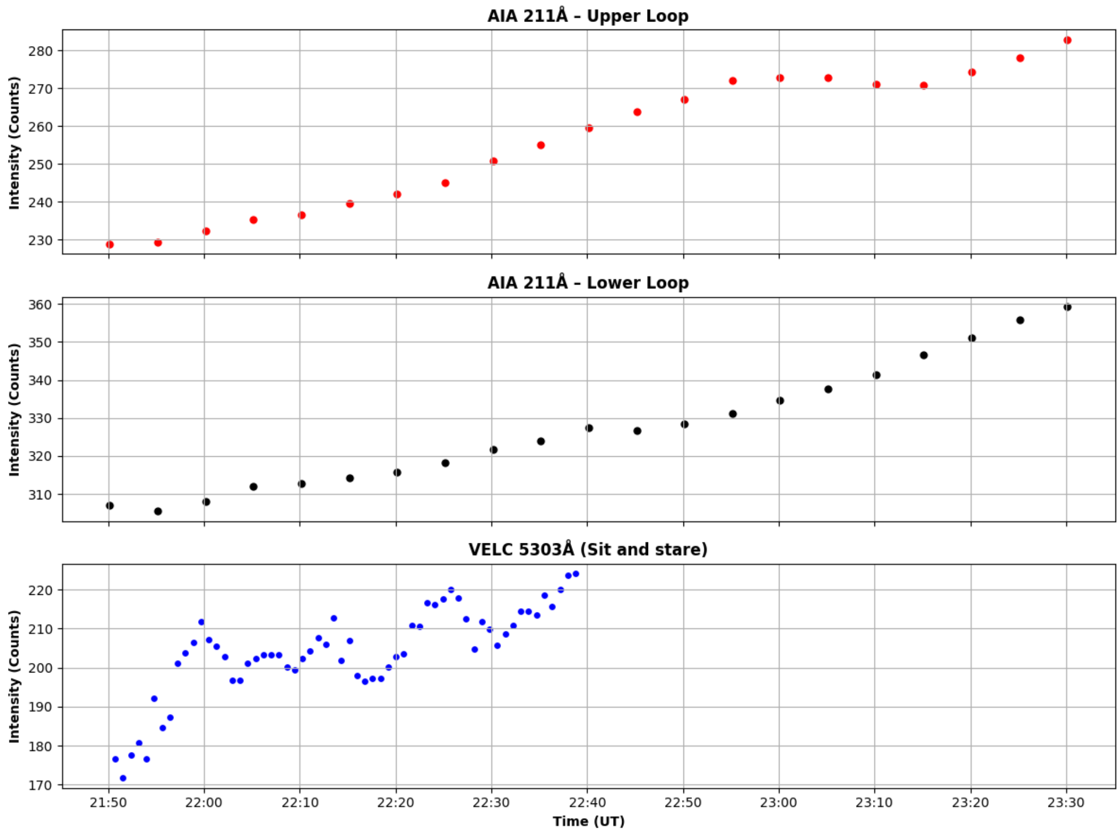

Figure 6. Temporal changes in the VELC 5303 Å sit-stare emission line intensity at the location of the coronal loop (lower panel) and SDO/AIA 211 Å intensity near the footpoints of the upper and lower legs of the loop (upper and middle panels, respectively).

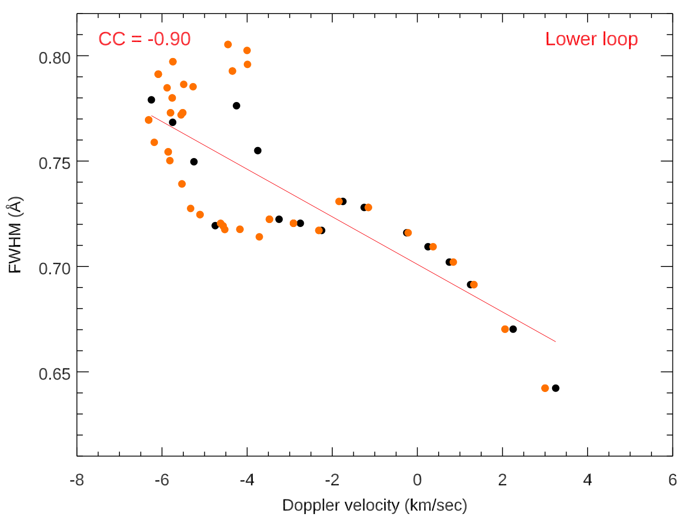

Figure 7. Scatterplot (orange color data points) of the Doppler velocities with the line widths (FWHM) in the lower leg of the coronal loop structure observed with the VELC (Figures 1, 3, and 4). Black data points correspond to Doppler velocities grouped into bins of 0.5 km s^{-1} and the average FWHM value corresponding to each bin. The correlation coefficient (CC) between the two parameters, obtained using the latter dataset, is −0.9. The CC in the case of the former (orange data points) is −0.79.

in the sign of the Doppler velocity due to the combination of unresolved flows. Based on simultaneous observations in multiple spectral lines using SDO/AIA and Hinode/EIS, S. W. McIntosh et al. (2012) pointed out that there can be cooling downflows and heating upflows within the resolution limit of the instrument. The downflows are dominant at lower temperatures, and upflows are dominant at higher temperatures. Hence, there can be a gradual change in the Doppler velocity, from redshift toward blueshift, with an increase in temperature. As mentioned in the previous paragraph, there is an increase in $T_{\rm eff}$ from $\approx$1.4 $\times$ 10^6 K at 1.1$R_\odot$ to $\approx$2.9 $\times$ 10^6 K at 1.24$R_\odot$, along the lower leg of the loop. The larger change in the Doppler velocity magnitude ($\gtrsim$11 km s^{-1}) is an unambiguous indication of the presence of bulk flows in the 5303 Å line (see, e.g., M. Mierla et al. 2008; Y. Zhu et al. 2024). It is possible that the outflow is coherent, and unidirectional. Note that the above value is for the LoS component alone. Considering this, and the near-limb location of the associated active region (Section 2.2), the total outflow velocity is expected to be comparatively larger.

As mentioned in Section 3.1, the emission line intensity in the upper leg of the loop shows a factor of ≈1.7 decrease between $\approx 1.10R_\odot$ and $\approx 1.14R_\odot$, likely due to the bright emission near the occulter edge in the upper leg (Figure 1). Thereafter, it remains almost steady until the loop apex at $\approx 1.24R_\odot$ (upper panel of Figure 4). In the case of the lower leg, the intensity is nearly uniform over the entire distance range, i.e., 1.10–$1.24R_\odot$. Since the density scale height for $T_e \approx 1.2 \times 10^6$ K is $\approx 0.086R_\odot$ (see, e.g., M. J. Aschwanden et al. 2001), the above steady behavior of the emission line flux along either legs of the loop in the present case is a likely indication of superhydrostatic scale height that can exceed up to 5 times the normal value (see, e.g., M. J. Aschwanden 2026). An exponential extrapolation of the line intensities in the upper leg of the loop, backward toward the solar limb, indicates that the intensity at $1R_\odot$ should be ≈45 erg s^{-1} cm^{-2} $Å^{-1}$ sr^{-1}. The corresponding scale height is $\approx 0.096R_\odot$, which agrees reasonably with that for $T_e \approx 1.2 \times 10^6$ K mentioned above. Strong inverse correlation (CC = −0.9) between the line width and Doppler velocity in only one of the loop footpoints, as in the present case (Figure 7), was reported earlier by R. O. Milligan (2011) from extreme-ultraviolet (EUV) observations. The authors attributed the excess broadening due to unresolved plasma flows along the LoS during the process of chromospheric evaporation by nonthermal electrons (see, e.g., D. Tripathi et al. 2012).

3.5. Alfvén Waves

Assuming the LoS depth (l) of the loop to be the same as its width (see, e.g., D. Li et al. 2020), we calculated the electron density (N_e) in the loop using the relation, $N_e = (\mathrm{EM}/l)^{0.5}$. EM is the emission measure, estimated using the relation $\mathrm{EM} = I(\lambda)/G(T, \lambda, N_e)$, where $I(\lambda)$ is the intensity of the emission line and $G(T, \lambda, N_e)$ is the contribution function obtained utilizing CHIANTI atomic database (K. P. Dere et al. 1997, 2023).[2] Inferring $N_e = 10^8$ cm^{-3} for the "background" corona at $r \approx 1.06R_\odot$ (G. Del Zanna & E. E. DeLuca 2018), we calculated $G(T, \lambda, N_e)$ for $T = 1.2 \times 10^6$ K and $\lambda = 5303$ Å as 5.99×10^{-28} erg s^{-1} cm^{-3} sr^{-1}. The observed intensity values at $\approx 1.10R_\odot$ are ≈16.5 erg s^{-1} cm^{-2} $Å^{-1}$ sr^{-1} in the upper loop and ≈8.1 erg s^{-1} cm^{-2} $Å^{-1}$ sr^{-1} in the lower loop (Figure 3). Using the above values, we computed EM for the upper and lower legs of the loop at $\approx 1.10R_\odot$. The values are $\approx 2.75 \times 10^{28}$ cm^{-5} and $\approx 1.35 \times 10^{28}$ cm^{-5}, respectively. These are upper limits at the above temperature T since the observations are in a single emission line (G. Del Zanna 2013). The width of the upper and lower loop at $\approx 1.10R_\odot$ are $l \approx 6.1 \times 10^9$ cm and $l \approx 3.2 \times 10^9$ cm (Figure 1, right panel). The N_e values at $\approx 1.10R_\odot$ in the upper and lower legs, calculated using the above numbers, are the same for both loops, $\approx 2.1 \times 10^9$ cm^{-3}. The energy flux density of the Alfvén waves is $F = \rho^{1/2} v_{\mathrm{nt}}^2 B/\sqrt{\pi}$, where $\rho = m_p N_e$ is the mass density, $m_p = 1.67 \times 10^{-24}$ g is the mass of proton, v_{nt} is the nonthermal velocity, and B is the strength of the magnetic field (see, e.g., J. G. Doyle et al. 1998). Assuming $B \approx 16$ G at $1.10R_\odot$ (G. A. Dulk & D. J. McLean 1978), and $v_{\mathrm{nt}} \approx 27$ km s^{-1} (upper leg) and ≈19 km s^{-1} at $1.1R_\odot$ (lower leg) for the loop as mentioned previously, we get $F \approx 3.9 \times 10^6$ erg cm^{-2} s^{-1} and $F \approx 1.9 \times 10^6$ erg cm^{-2} s^{-1} at $1.1R_\odot$ for the two legs of the loop, respectively. The usually quoted energy loss from a coronal active region is 10^7 erg cm^{-2} s^{-1} (G. L. Withbroe & R. W. Noyes 1977). This suggests that in the present case, Alfvén waves may supply ≈19%–39% of the energy required to heat the corona. The actual contribution might be still less since EM and hence, N_e mentioned above, are upper limits. B can be also much smaller, ≈4 G at $1.1R_\odot$ (see, e.g., H. Lin et al. 2004). The emission line width near the loop apex is expected to be smaller than that near the footpoint in the case of an edge-on loop if the nonthermal width of the emission line is due to Alfvén waves (see, e.g., H. Hara & K. Ichimoto 1999). The present observations are different. The loop appears face-on. Further, the FWHM of the emission line along the lower leg of the loop increases toward the apex of the loop. In the case of the upper leg, the FWHM remains more or less uniform (middle panel in Figure 4).

4. Summary

We have reported variations in the parameters of the 5303 Å emission line with height above the solar limb (r = 1.10–$1.24R_\odot$) for a preflare coronal loop using Aditya-L1/VELC observations in the raster scan mode. There was a C1.9 class GOES soft X-ray flare from the same active region, 13 minutes after the VELC observations were over. The width and Doppler velocity of the line show significant changes (≈0.2 Å and 11 km s^{-1}, respectively) in one of the legs of the loop. The changes are ≈90% inversely correlated. The Doppler velocity shows blueshift. The observations provide clear evidence for simultaneous line broadening and plasma upflows along the coronal loop in 5303 Å, likely due to energy releases associated with the preflare activities at the footpoint of the loop. Estimates of the Alfvén wave energy flux densities indicate that the upper limits for the corresponding values in the two legs of the loop at $r \approx 1.1R_\odot$ are $\approx 3.9 \times 10^6$ erg cm^{-2} s^{-1} and $\approx 1.9 \times 10^6$ erg cm^{-2} s^{-1}, which are ≈39% and ≈19% of the energy required to heat the corona (10^7 erg cm^{-2} s^{-1}) in the active regions. We intend to carry out more studies with the VELC to verify the above results.

Acknowledgments

The VELC team members who developed the payload are thanked for their efforts. Aditya-L1 is an observatory class mission, funded and operated by the Indian Space Research Organization (ISRO). Data obtained with the different payloads on board Aditya-L1 are archived at the Indian Space Science Data Centre (ISSDC) of ISRO. We acknowledge the SDO/AIA team for providing open data access. CHIANTI is a collaborative project involving the University of Cambridge (UK), the NASA Goddard Space Flight Center (USA), the George Mason University (GMU, USA), and the University of Michigan (USA). We are thankful to the referee for kind and insightful comments that helped to present our results more clearly.

ORCID iDs

R. Ramesh https://orcid.org/0000-0003-2651-0204
V. Muthu Priyal https://orcid.org/0000-0001-6093-3302
Jagdev Singh https://orcid.org/0000-0003-0562-2979
K. Sasikumar Raja https://orcid.org/0000-0002-1192-1804

[2] https://www.chiantidatabase.org/

References

Aschwanden, M. J. 2026, SoPh, 301, 66
Aschwanden, M. J., Poland, A. I., & Rabin, D. M. 2001, ARA&A, 39, 175
Boe, B., Habbal, S. R., Druckmüller, M., et al. 2020, ApJ, 888, 100
Boe, B., Habbal, S. R., Druckmüller, M., et al. 2026, ApJ, 997, 171
Bruzek, A., & Demastus, H. L. 1970, SoPh, 12, 447
Budihal, R. P., Narra, V. S, Venkatasubramanian, N., et al. 2023, JATIS, 9, 044001
Chitta, L. P., Peter, H., & Solanki, S. K. 2018, A&A, 615, L9
Contesse, L., Koutchmy, S., & Viladrich, C. 2004, AnGeo, 22, 3055
Del Zanna, G. 2013, A&A, 558, A73
Del Zanna, G., & DeLuca, E. E. 2018, ApJ, 852, 52
Del Zanna, G., & Mason, H. E. 2003, A&A, 406, 1089
Dere, K. P., Del Zanna, G., Young, P. R., & Landi, E. 2023, ApJS, 268, 52
Dere, K. P., Landi, E., Mason, H. E., Monsignori Fossi, B. C., & Young, P. R. 1997, A&AS, 125, 149
Ding, A., & Habbal, S. R. 2017, ApJL, 842, L7
Doschek, G. A., Warren, H. P., Mariska, J. T., et al. 2008, ApJ, 686, 1362
Doyle, J. G., Banerjee, D., & Perez, M. E. 1998, SoPh, 181, 91
Dulk, G. A., & McLean, D. J. 1978, SoPh, 57, 279
Grotrian, W. 1939, NW, 27, 214
Hara, H., & Ichimoto, K. 1999, ApJ, 513, 969
Hara, H., Watanabe, T., Harra, L. K., et al. 2008, ApJL, 678, L67
Hori, K., Ichimoto, K., Sakurai, T., Sano, I., & Nishino, Y. 2005, ApJ, 618, 1001
Kim, I. S. 2000, ASPC, 205, 69
Koutchmy, S., Baudin, F., Abdi, S., Golub, L., & Sévre, F. 2019, A&A, 632, A86
Krishna Prasad, S., Singh, J., & Banerjee, D. 2013, SoPh, 282, 427
Landi, E., Habbal, S. R., & Tomczyk, S. 2016, JGRA, 121, 8237
Lemen, J. R., Title, A. M., Akin, D. J., et al. 2012, SoPh, 275, 17
Li, D., Yuan, D., Goossens, M., et al. 2020, A&A, 639, A114
Lin, H., Kuhn, J. R., & Coulter, R. 2004, ApJL, 613, L177
Martin, S. F. 1980, SoPh, 68, 217
McIntosh, S. W., Tian, H., Sechler, M., & De Pontieu, B. 2012, ApJ, 749, 60
Mierla, M., Schwenn, R., Teriaca, L., Stenborg, G., & Podlipnik, B. 2008, A&A, 480, 509
Milligan, R. O. 2011, ApJ, 740, 70
Muro, G. D., Gunn, M., Fearn, S., Fearn, T., & Morgan, H. 2023, SoPh, 298, 75
Muthu Priyal, V., Ramesh, R., Singh, J., & Sasikumar Raja, K. 2025a, ApJ, 983, 171
Muthu Priyal, V., Ramesh, R., Singh, J., Sasikumar Raja, K., & Gopalswamy, N. 2025b, ApJ, 994, 182
Muthu Priyal, V., Singh, J., Prasad, B. R., et al. 2024, AdSpR, 74, 547
Ramesh, R., Muthu Priyal, V., Singh, J., & Sasikumar Raja, K. 2025, SoPh, 300, 165
Ramesh, R., Muthu Priyal, V., Singh, J., et al. 2024, ApJL, 976, L6
Sakurai, T., Ichimoto, K., Raju, K. P., & Singh, J. 2002, SoPh, 209, 265
Singh, J., Hasan, S. S., Gupta, G. R., Nagaraju, K., & Banerjee, D. 2011, SoPh, 270, 213
Singh, J., Prasad, B. R., Venkata, S., & Kumar, A. 2019, AdSpR, 64, 1455
Singh, J., Ramesh, R., Prasad, B. R., et al. 2025, SoPh, 300, 66
Singh, J., Sakurai, T., & Ichimoto, K. 2006a, ApJ, 639, 475
Singh, J., Sakurai, T., Ichimoto, K., & Muneer, S. 2006b, JApA, 27, 115
Singh, J., Sakurai, T., Ichimoto, K., & Watanabe, T. 2004, ApJL, 617, L81
Suzuki, I., Sakurai, T., & Ichimoto, K. 2006, PASJ, 58, 165
Tian, H., Tomczyk, S., McIntosh, S. W., et al. 2013, SoPh, 288, 637
Tripathi, D., Mason, H. E., Del Zanna, G., & Bradshaw, S. 2012, ApJL, 754, L4
Tsubaki, T. 1975, SoPh, 43, 147
Tsubaki, T. 1983, SoPh, 87, 57
Withbroe, G. L., & Noyes, R. W. 1977, ARA&A, 15, 363
Young, C. A. 1872, Natur, 159, 28
Zhu, B. Q., Xu, Z., & Xiang, C. 2025, MNRAS, 540, 2641
Zhu, Y., Habbal, S. R., Ding, A., et al. 2025, ApJ, 966, 122